Journal Pre-proof

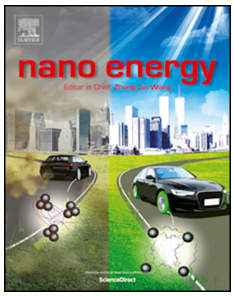

Photochemically deposited Ir-doped NiCo oxyhydroxide nanosheets provide highly efficient stable electrocatalysts for the oxygen evolution reaction

Liang-ai Huang, Hyeyoung Shin, William A. Goddard, III, Jianming Wang

PII: S2211-2855(20)30442-0

DOI: https://doi.org/10.1016/j.nanoen.2020.104885

Reference: NANOEN 104885

To appear in: *Nano Energy*

Received Date: 16 February 2020

Revised Date: 25 March 2020

Accepted Date: 23 April 2020

Please cite this article as: L.-a. Huang, H. Shin, W.A. Goddard III., J. Wang, Photochemically deposited Ir-doped NiCo oxyhydroxide nanosheets provide highly efficient stable electrocatalysts for the oxygen evolution reaction, *Nano Energy* (2020), doi: https://doi.org/10.1016/j.nanoen.2020.104885.

The contributions of the authors are as follows.

Liang-ai Huang: Experimental Investigations, experimental Methodology, Writing- paper

Hyeyoung Shin: computations, writing of computational parts and of discussion

William A. Goddard III: Conceptualization of computations, writing of computational parts and of discussion

Jianming Wang: Conceptualization of experiments, Writing- Reviewing and Editing of experimental section, Supervision of experiments

Photochemically deposited Ir-doped NiCo Oxyhydroxide Nanosheets provide Highly Efficient and Stable Electrocatalysts for the Oxygen Evolution Reaction

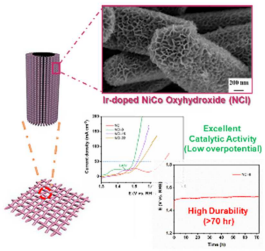

Photochemically deposited Ir-doped NiCo Oxyhydroxide Nanosheets provide Highly Efficient Stable Electrocatalysts for the Oxygen Evolution Reaction

Liang-ai Huang,[+,a] Hyeyoung Shin,[+,b,c] William A. Goddard III,[*,b] and Jianming Wang,[*,a]

[a]Department of Chemistry, Zhejiang University, Hangzhou 310027, PR China

[b]Materials and Process Simulation Center (MSC) and Joint Center for Artificial Photosynthesis (JCAP), California Institute of Technology, Pasadena, California 91125, USA

[c]Graduate School of Energy Science and Technology (GEST), Chungnam National University, 99 Daehak-ro, Yuseong-gu, Daejeon 34134, Republic of Korea

[+]These authors contributed equally to this work.

* To whom all correspondences should be addressed

E-mail) wjm@zju.edu.cn, wag@caltech.edu

Abstract

To achieve practical production of fuel from water, it is essential to develop efficient and durable electrocatalysts for the oxygen evolution reaction (OER). We report here that doping NiCo-OOH nanosheets with 8% Ir leads to a low overpotential of only 260 mV for 50 mA/cm^2, far better than previous OER catalysts. We synthesized this catalyst using a novel photochemical deposition method that leads to a uniform distribution of dopant, large catalytic active area, high interfacial charge transfer efficiency, good adhesion between catalyst and matrix, and long lifetime. Moreover, these nanosheets show significant stable performance for 70 hours in alkaline media. Our density functional theory calculations, show that Ir and Co both play essential bifunctional roles in stabilizing the key O radical intermediate on Ir and promoting the O-O bond coupling on Co, which is optimum for the 8% Ir.

Keywords: Oxygen Evolution Reaction; NiOOH Oxyhydroxide; Density Functional Theory; Photodeposition; Reaction Mechanism;

1. Introduction

The oxygen evolution reaction (OER) plays an important role in such energy conversion systems as water splitting, CO_2 reduction, and metal-air batteries [1-3]. Recently, great efforts have been devoted to developing OER catalysts with improved performance [4]. However, sluggish kinetics due to a high overpotential for the complex four-electron coupled process have remained as obstacles to making the electrochemical system more efficient. This makes identification of active and efficient electrocatalysts for high OER performance a priority. IrO_2 has been regarded as promising OER catalyst in acid media due to its low overpotential and high catalytic performance. However, its high cost and instability in base hinder its commercial applications. Thus, it is imperative to identify and characterize new low cost electrocatalysts that provide more efficient and durable electrocatalytic properties.

Among various transition metal oxide based OER electrocatalysts, Nickel oxyhydroxides (NiOOH) have shown promising electrocatalysis toward OER in alkaline medium with enhanced electrochemical activity, earth abundance nature, and open structure [5-7]. Thus γ-NiOOH is known to be the active phase for OER, with a formal Ni valence of about +3.6 [8]. Several studies have shown that incorporation of other metals in NiOOH can further improve OER catalytic activity [9]. In particular, Fe-doped γ-NiOOH oxyhydroxides (Fe-γ-NiOOH) have been recognized as most active non-precious electrocatalyst for OER under alkaline condition, leading to excellent catalytic performance and prominent stability [10]. However, Fe-γ-NiOOH is far from adequate. To design better electrocatalyst, Boettcher showed experimentally that NiCo-based oxyhydroxides (NiCoOOH) enhance catalytic performance over NiFe-based oxyhydroxides because the electronic conductivity of CoOOH is far superior to that of FeOOH [11]. Previous studies also found improvements for Mo- and Fe-doped NiOOH [5]. However, the OER performance of bulk NiCoOOH remains unsatisfactory due to its low specific surface area and sluggish interface charge transfer. Moreover, the semiconductor properties of pristine NiCoOOH greatly impede charge transfer from the catalyst to the supporting substrate, limiting catalytic activity and overall efficiency for the OER [12-14]. Recently, *in-silico* screening by Shin and Goddard predicted that Co-, Rh-, and Ir-doping of NiOOH would improve OER electrocatalysis, with particularly dramatic improvement for Ir [15]. Therefore, we developed new materials synthesis strategies for Ir-doped NiCoOOH catalyst aiming at boosting OER catalytic activity.

In addition to enhancing the catalytic activity, it is also important to design the catalyst to obtain a large active surface area and good structural stability. Constructing free-standing nanostructures can provide large electrochemical active area while strengthening the adhesion interaction between catalyst and substrate can improve the structural stability of the catalyst. To accomplish this, we developed a **novel photochemical deposition method** that has prominent advantages of **uniform distribution, high interfacial charge transfer efficiency, good adhesion between catalyst and matrix** while saving energy in fabricating the Ir-doped NiCoOOH catalyst. Our photochemical deposition method utilizes the strong oxidizing properties of photo-generated holes. We show that under stimulation by UV-vis light, photogenerated holes are transferred to the semiconductor surface leading to oxidation of metal ions and in-situ deposition on its surface, thus greatly strengthening the combination between the catalyst and the substrate. This contrasts with the photochemical preparation method of the Berlinguette group, who uses photochemical decomposition to fabricate OER catalysts [16-18].

Based on these considerations, we first designed a hierarchical layered Ir-doped NiCoOOH catalyst supported on ZnO/nitrogen-doped carbon cloth substrate, which is fabricated successfully through our novel photochemical deposition method. Under light stimulation the Ni^{2+}, Co^{2+} and Ir^{3+} were all oxidized by the strong oxidizing property of the photo-induced holes so that the electrocatalyst is uniformly deposited in-situ on the outer surface of the *n*-type semiconductor ZnO. Our electrochemical tests show that the Ir-doped NiCoOOH electrode with 8% Ir exhibits excellent catalytic performance, requiring an **overpotential of only 260 mV to achieve a current of 50 mA cm^{-2},** which is superior to previous electrocatalysts for OER. Moreover, our photochemical based synthetic method leads to large surface area and increased stability (70 hours with only 3% change in performance).

We find that the excellent catalytic performance of the Ir-doped NiCoOOH/ZnO composite arises mainly from three aspects:

i) photochemical deposition ensures strong bonding between the catalyst and the substrate, which facilitates the construction of free-standing nanostructures having large electrochemical active area to improve activity and structure stability;

ii) the hierarchical porous structures expose more surface area of the catalyst, providing increased active sites while promoting full contact with the electrolyte to facilitate charge transfer;

iii) the Ir dopant on oxyhydroxides / oxides plays a pivotal role in promoting OER active sites while modifying the electronic structure to greatly reduce the catalyst overpotential to accelerate charge transfer, boosting catalytic performance.

To understand the origin of dramatically improved performance due to Ir doping on the NiCoOOH surface, we applied density functional theory (DFT). This confirmed that the catalyst with 8% Ir exhibits the best performance with the Ir facilitating formation of IrO oxo bond with radical character on the O and the Co facilitating the O-O formation step.

2. Experimental section

2.1. Synthesis of ZnO NRAs@NCC

The chemical reagents used were all analytical grade, without further purification. To improve the hydrophilicity of carbon cloth, it was surface-functioned using concentrated HNO3 for 24 h at 90 ºC, then rinsed several times with deionized water, and dried at 60 ºC under vacuum. This N-doping treatment increases the roughness and the electronic con-ductivity of the carbon cloth. The fabrication of nitrogen-doped carbon cloth (NCC) in-volves three steps: followed by hydrothermal reaction, thermal reduction, and concentrat-ed acid treatment, as described in the related investigations of Tong and coworkers [19]. The growth of ZnO nanorod arrays on NCC was carried out with the following steps. First, a piece of NCC (1 cm × 1.5 cm) was immersed in the seeding solution containing 0.01 M $Zn(CH_3COO)_2 \cdot 2H_2O$ and 0.01 M NaOH, followed by hydrothermal treatment at 150 ºC for 15 min. The above seeding process was repeated four times. After that, the growth solution of 0.10 M hexamethylenetetramine (HMTA) and 0.10 M $Zn(NO_3)_2 \cdot 6H_2O$ were dissolved in deionized water separately at room temperature, then mixed and stirred for 30 min. Then the NCC covered with the ZnO seed layer and the growth solution were transferred together to a Teflon-lined stainless steel autoclave and heated at 100 ºC for 12 h. The obtained greyish-white film was rinsed extensively with deionized water and finally annealed in a pipe furnace

at 400 ºC for 1 h under the flow of Ar to obtain the ZnO NRAs@NCC substrate.

2.2. Preparation of the Ir-doped NiCoOOH/ZnO@NCC composite film

The Ir-doped NiCoOOH/ZnO@NCC composite films were fabricated through a novel photochemical deposition method. The photodeposition solution consisted of 0.13 M $NiSO_4 \cdot 6H_2O$, 0.10 M $CoCl_2 \cdot 6H_2O$, 0.13 M CH_3COONa with a series of molar concentrations of $IrCl_3 \cdot xH_2O$ (Ir>52%). The ZnO NRAs@NCC substrate and the Pt electrode were placed into the photodeposition reactor and connected by a wire for short-circuit. The ZnO NRAs@NCC substrate was placed opposite the UV-vis light irradiation (500 W Xe lamp, 2.0 mW cm^{-2}) through the quartz window, and its exposed area was 1 cm^2, the photodeposition process is displayed in Figure S1. In the process of photodeposition, the solution was stirred constantly to ensure the stability and uniformity of the deposition system. The composite film obtained after 3 hours of photodeposition exhibits the best catalytic activity. After the deposition, the as-fabricated composite film was rinsed with deionized water several times and vacuum dried at 60 ºC.

The preparation process of NiCoOOH/ZnO@NCC composite film was the same as for the Ir-doped NiCoOOH/ZnO@NCC, except that there is no $IrCl_3 \cdot xH_2O$ in the photodeposition solution. We denote the Ir-doped NiCoOOH/ZnO@NCC composite films as NCI-x%, where x is the atomic ratio of Ir content among all metals (Ni, Co, Ir), and the value of x is determined by the ICP analysis. These atomic ratios are displayed in Table S1. Similarly, NI-x% indicates the individual doping of Iridium into NiOOH, where x refers to the Ir content. NiCoOOH/ZnO@NCC is described as NC.

2.3. Physical characterization

The crystalline structures of the fabricated film samples were characterized by X-ray diffraction (XRD) on the D/MAX 2550 X ray diffractometer from Rigaku company using Cu Kα radiation. Scanning electron microscopy (SEM, Carl Zeiss, Ultra 55) at an acceleration voltage of 5 kV and high-resolution transmission electron microscopy (TEM, Tecnai G2 F30) with an accelerating voltage of 200 kV were used to observe the morphologies and microstructures of the films. X-ray photoelectron spectroscopy (XPS) data were recorded using the Escalab 250Xi X-ray physical electronics photoelectron spectrometer with Mg Kα radiation. The obtained spectra were corrected according to the adventitious C 1s peak (284.6 eV). The atomic ratios of the Ni, Co, Ir elements of the as-fabricated composite films were analyzed using inductively coupled plasma atomic emission spectroscopy (ICP, SPECTRO). The as-fabricated samples were dissolved in nitric acid solution, and the resulted solutions were used for ICP analysis.

2.4. Electrochemical measurements

Electrochemical measurements of the catalysts were carried out using a three-electrode system on a CHI660D electrochemical workstation at room temperature. The as-prepared NCI composite film was used as the working electrode, while Ag/AgCl electrode (filled with saturated KCl solution purchased from Rex company) and platinum foil were utilized as the reference electrode and the counter electrode, respectively. 1 M KOH aqueous solution was employed as an electrolyte. The Ag/AgCl electrode calibration was carried in a three-electrode system with Pt foil as working counter electrode and Ag/AgCl as reference electrode. The electrolyte was H_2 saturated 1.0 M KOH. The LSV curve was collected at 5 mV/s scan rate, and the potential at which the current crosses zero was taken as thermodynamic potential (vs Ag/AgCl) for the hydrogen electrode [20]. The potential at

which current crosses zero is -1.027 V vs Ag/AgCl, as shown in Figure S2, so all potentials were calibrated according to the equation: $E_{RHE} = E_{Ag/AgCl} + 1.027$. The electrocatalytic activity of the NCI composite film was measured by linear sweep voltammetry (LSV) at a scan rate of 5 mV s^{-1} with 95% *iR* drop compensation. The stability performance of the NCI composite film was tested using chronopotentiometry at a current density of 20 mA cm^{-2}. Cyclic voltammetry (CV) was carried out at a scan rate of 5 mV s^{-1} in the potential range of 0.2 to 0.9 V vs. Ag/AgCl. Electrochemical impedance spectroscopy (EIS) was conducted within the frequency range of 100 kHz to 0.01 Hz to obtain the solution impedance (R_s) of the electrochemical system and investigate the kinetics of the electrocatalysts under OER conditions. The electrochemical active surface area (ECSA) was determined on the basis of the measured double-layer capacitance (C_{dl}), which was calculated by CV curves within a potential range of 0.1 V centered at open-circuit potential at different scan rates.

2.5. Computational details

We carried out spin-polarized density functional theory (DFT) calculations using the Vienna Ab-initio Simulation Package (VASP) [21] for the investigation of the atomistic mechanisms for OER on the NCI surfaces. We used the Perdew-Burke-Ernzerhof (PBE) flavor of DFT [22] including the D3 empirical van der Waals correction with Becke-Johnson parameters. The projector augmented wave (PAW) potentials [23] were used to describe the valence electron-ion interactions. This level correctly describes the adsorption energies of intermediates on a variety of surfaces [24-26].

For the geometry optimizations, we used a plane-wave energy cutoff of 400 eV. We employed a gamma-centered Monkhorst k-point mesh of (3×3×1). All surface models were built by including an additional vacuum region of 15 Å. The bottom two layers of the slabs were fixed at the lattice spacing of the bulk while the top two layers were allowed to optimize. Dipole corrections were applied to the surface normal direction. Here, the solvation was included by introducing explicit H_2O molecules on the surface.

For the calculation of free energy for each step at room temperature (298.15 K), we computed the zero-point energies, enthalpy, and entropy based on the vibrational frequencies.

3. Results and discussion

3.1. Synthesis, structure and composition of materials

The fabrication of the hierarchical layered NCI composite film is displayed schematically in Fig. 1. The ZnO nanorod arrays were initially grown on NCC through the hydrothermal reaction using zinc acetate, sodium hydroxide, hexamethylenetetramine and zinc nitrate as precursors. Subsequent heat treatment was carried out in an Ar atmosphere in order to improve the crystallinity of ZnO nanorod arrays. After that, the strong oxidizing properties of photogenerated holes, were used to oxidize the metal ions (Ni^{2+}, Co^{2+}, Ir^{3+}) to obtain hierarchical layered NCI composite film. It is important to note that the uniformly hierarchical nanorod structure of the ZnO can effectively disperse the catalytically active materials and fully expose the catalytically active sites of the NCI electrocatalysts.

The XRD patterns of the as-fabricated NC, NCI-8, NCI-15 and NCI-22 composite films are shown in Fig. 2 and Fig. S3. All diffraction peaks of the as-fabricated samples match well with ZnO (JCPDS Card No. 01-070-8070) or carbon cloth (JCPDS Card No. 00-037-0474), with no other peaks, indicating the amorphous structure of the as-synthesized electrocatalysts.

We expect that only a small driving force is required to transform the oxygen-evolving state from an amorphous structure into an ordered structure, explaining the high catalytic activity of the amorphous catalyst [27].

The Raman spectra of the as-prepared NC, NCI-8, NCI-15 and NCI-22 composite films are displayed in Fig. S4. The peaks located at 305 and 335 cm^{-1} can be assigned to Ir-OH signals [28], and the weak peak observed at 561 cm^{-1} is the characteristic Raman Ir-O stretch mode [29-30], indicating a Ir-OOH phase. The sharp peak observed at 440 cm^{-1} is attributed to the E2 (high) vibration modes of ZnO [31-32], which is consistent with the XRD results. Furthermore, the broad Raman band located at 587 cm^{-1} can be assigned to CoOOH (Co(IV)) species [30,33], and the other two peaks centered at 475 and 550 cm^{-1} correspond to Ni-O vibrations in γ-NiOOH [34-36]. However, it is clear that these two peaks shift to 538 cm^{-1} with incorporation of Ir.

The microstructures of NCI-8 were characterized by using SEM, TEM, and HRTEM, as shown in Fig. 3. NCI-8 is grown uniformly on regular hexagonal prism ZnO nanorods (Fig. S5) with hierarchical arrays consisting of interlaced nanosheets, as shown in Fig. 3a-c. The thickness of the nanosheets is measured to be about 5 nm. The SEM images of the as-fabricated NC, NCI-15 and NCI-22 with different amounts of Ir dopant are displayed in Fig. S6, showing nanosheet array structures similar to NCI-8. The TEM images in Fig. 3d-e further demonstrate that the ZnO nanorods are evenly coated with hierarchical nanosheets, and the interconnected nanosheets are stacked to form hierarchical porous structures. In addition, visible dark strips are folded edges or wrinkled nanosheets, which show their ultrathin nature. The lattice spacing of 2.48 Å in the HRTEM images (Fig. 3f and Fig. S7a) can be indexed to the (101) crystal plane of ZnO, but no other obvious lattice space can be observed. The corresponding SEAD pattern of amorphous layer is displayed in Fig. S7b, which further confirms the existence of ZnO in the composite and the amorphous structure of NCI-8 nanosheets. This is in accordance with the XRD results. The elemental mappings of NCI-8 in Fig. 3g show that the elements Ni, Co, Zn, O and Ir are well-dispersed and the Ir content is relatively low. The comparative NC composite film exhibits the similar microstructures to NCI-8, as shown in Fig. S8a-b, and its HRTEM image (Fig. S8c) indicates the presence of ZnO substrate and the weak crystalline catalyst layer. The original amorphous layer has weak lattice stripes due to the rearrangement of the amorphous disordered structure by high-energy electrons in the detection environment. The elemental mappings of NC (Fig. S9) show the homogeneous distributions of elements Ni, Co, Zn and O.

X-ray photoelectron spectroscopy (XPS) measurements were conducted to further investigate the valence state and element composition of the as-fabricated NCI-8 composite film. In the high-resolution Ir *4f* spectrum in Fig. 4a, two main peaks of Ir $4f_{7/2}$ and Ir $4f_{5/2}$ can be deconvoluted into Ir^{3+} and Ir^{4+} [37], and two bands at 61.8 and 64.9 eV correspond to Ir^{3+}, while the Ir^{4+} peaks are located at 62.8 and 65.8 eV. But after OER, the spectrum shows a significant shift toward higher binding energy, which indicates that some of the Ir^{3+}/Ir^{4+} have been further oxidized to Ir^{5+} species [38-39], which is consistent with the results of the CV test in Fig. 5c. Fig. 4b shows the high-resolution XPS pattern of the Ni *2p* spin-orbit splitting of NCI-8. The Ni $2p_{3/2}$ and Ni $2p_{1/2}$ peaks can be deconvoluted into peaks of Ni^{3+} and Ni^{4+}, where the characteristic peaks at about 855.8 and 873.6 eV can be identified as Ni^{3+} species, whereas the other two peaks centered at 857.9 and 875.6 eV can be attributed to Ni^{4+} species. After OER, the proportion of Ni^{4+} has increased significantly, as some of the Ni^{3+} are oxidized to Ni^{4+}, leading to a final formal Ni valence is about 3.52, which is in line with the average valence of the reported γ-NiOOH [40]. The high-resolution Co 2p XPS spectrum of

the as-fabricated NCI-8 is given in Fig. 4c, showing a pair of Co $2p_{3/2}$ and Co $2p_{1/2}$ doublet peaks, which can also be deconvoluted into peaks of Co^{3+} and Co^{4+}. The as-deconvoluted peaks centered at 781.0 and 796.5 eV correspond to Co^{3+} species, while the peaks with the binding energies at 783.5 and 798.3 eV are ascribed to Co^{4+} species [41]. Similarly, the ratio of Co^{4+} has increased significantly after OER, causing Co species to exhibit a higher valence state. The wide-scan survey spectra of NC, NCI-8, NCI-15 and NCI-22 composite films are displayed in Fig. S10, revealing the successful photochemical depositions of NC and NCIs on the final composite films, respectively. The high-resolution Ni *2p*, Co *2p* and Ir *4f* XPS patterns of NC, NCI-8, NCI-15 and NCI-22 composite films after OER tests are shown in Figs. S11, S12 and S13, respectively. Compared to the NC sample, the Ni *2p* XPS peaks of NCI-8, NCI-15 and NCI-22 all shift to a higher binding energy, indicating a strong electronic interaction between Ir dopant and NiCoOOH. In addition, Figs. S12 and S13 show that the Co *2p* peaks and Ir *4f* peaks of NCI-8 have the highest binding energy compared with the other as-fabricated electrocatalysts. Thus both the Co species and the Ir species exhibit the highest average valence state for NCI-8, the most active for OER [8-9,42].

3.2. Electrocatalytic activity of catalysts

In order to evaluate the effect of Ir doping, the OER catalytic activity of NCI electrodes with different atomic ratio of Ir content of 0, 8%, 15% and 22% (NC, NCI-8, NCI-15 and NCI-22, respectively) were measured via a standard three-electrode system by linear sweep voltammetry (LSV) in 1.0 M KOH with a scan rate of 5 mV s^{-1}. As indicated in the LSV curves of the various as-fabricated samples after *iR* correction (Fig. 5a), it is clear that NCI-8 exhibits the highest catalytic activity. It requires only an overpotential of only ~260 mV at 50 mA cm^{-2}, in contrast to NC, NCI-15, and NCI-22, which show much larger overpotentials of 448, 290 and 310 mV, respectively. Since the surface metal (Ni, Co and Ir) oxidation is accompanied by the OER process, to eliminate the contribution of any transient responses, we measured the catalytic activity of the as-fabricated samples using multi-potential step measurements, as shown in Fig. S14. For a more rigorous experimental design, we also fabricated two other catalysts, NCI-4 and NCI-11, whose OER performance are shown in Fig. S15. Clearly NCI-4 and NCI-11 exhibit poorer OER performance than NCI-8, indicating that a slight change in the content of Ir has a significant impact on the OER performance of the NCI catalyst.

NI-8 (Fig. S16) shows dramatically improved OER performance with overpotentials of 290 mV at 50 mA cm^{-2}, which can be compared to an overpotential of 445 mV at 50 mA cm^{-2} for NiOOH. This shows that the Ir doping plays a key role in enhancing catalytic activity of NiOOH. This validates the DFT predictions made earlier by Shin, Xiao, and Goddard [15]. Comparing the activities of NCI-8 and NI-8, we see that Co doping is also important in promoting OER activity, which we ascribe to **synergistic effects, with Ir stabilizing the radical O character and Co stabilizing O-O bond formation while Ni stabilizes the overall structure.**

The kinetics of OER process of all as-fabricated samples are evaluated by Tafel plots (overpotential vs. log *j*) derived from their polarization curves, as displayed in Fig. 5b. The Tafel slope of NCI-8 is about 72 mV/dec, which is significantly lower than that of NiOOH (224 mV/dec), NC (198 mV/dec), NCI-15 (134 mV/dec) and NCI-22 (163 mV/dec), demonstrating its superior intrinsic activity and more favorable electrocatalytic kinetics toward OER. However, we also observe that the Tafel slope of NI-8 (80 mV/dec) (Fig. S16) is only a little larger than that of NCI-8, further illustrating the critical role of Ir doping.

In order to illustrate the intrinsic activity of the as-fabricated film catalysts, we obtained the mass activity and turnover frequency (TOF) of the film samples. The average loadings of the NC, NCI-8, NCI-15 and NCI-22 catalysts on substrates ($1cm^2$) were about 0.32, 0.37, 0.39 and 0.40 mg, respectively. The mass activity of the NCI-8 film sample was over twice as high as the other films (see Fig. S17). The TOF reflects the intrinsic activity of the catalyst, but the number of active sites is difficult to determine, especially in heterogeneous catalytic systems. The simplest method is to take every metal cation as the "active site" and use the total film mass to determine the moles of metal in the film [11,43-44]. Therefore, total-metal TOF (TOF_{tm}) is defined as:

$$TOF_{tm}\ (s^{-1}) = \frac{\frac{Current\ (A)}{4F\ (C/mol)}}{\frac{film\ mass\ (g)}{MW\ NiCoIrOOH\ (g/mol)}} \quad (1)$$

At η = 300 mV, the TOF_{tm} of the as-fabricated NC, NCI-8, NCI-15 and NCI-22 catalysts are calculated to be 0.0171, 0.0988, 0.0462 and 0.0335 s^{-1}, as displayed in Fig. S17. In addition, we note that our fabricated NCI-8 electrocatalyst exhibits excellent OER activity, superior to that previously reported on state-of-the-art catalytic Ni-Co-Ir, Co-Ir, Ni-Ir systems and electrodes. (Table S2).

3.3. Density functional theory calculations

In order to understand the origin of high OER activity and the roles of each component in NCI-8, we carried out DFT calculations using methods we applied previously for *in silico* studies to identify dopants to replace Fe in Fe-doped NiOOH [15]. We built the NCI-8 slab model shown in Fig. S18, based on the crystal structure of NI-8 model used previously [15].

We first considered all possible reaction steps for OER to find the lowest energy pathways for OER, as shown in Fig. 6. This includes every state associated with each oxidation step (losing one electron) coupled with deprotonation and every possible O-O bond formation state on each different surface element (Ir, Co and Ni). The final results for the predicted pathway having the lowest free energy for OER on NCI-8 are reported in Fig. 6. Here we note that the presence of Ir on the NCI surface facilitates formation of a O radical sites on the Ir oxo bond while Co facilitates O-O coupling, both essential for OER. This synergy lowers the overpotential for OER.

As shown in Fig. 6, sequential oxidation-deprotonation steps starting from the NCI-8 slab model (Fig. S18, state 1) (state 1 ➔ state 2 and state 2 ➔ state 3) lead to formation of the O radical (O•), key intermediate for OER on the surface Ir site. Our DFT spin analysis finds that the Ir is in the 5+ oxidation state, in good agreement with the Cyclic Voltammogram data in Fig. 5c. The reaction (step 2 ➔ 3) proceeds via deprotonation of the OH adsorbed on the Ir, an endothermic process requiring 0.49 eV. Next O-O coupling (state 3 ➔ state 4) is generated by interaction between the O• on Co and an additional H_2O introduced at oxidation step 3, hydrogenating O on the Ir^{5+} site. Interestingly the O-O coupling prefers the Co site (requiring 1.18 eV for O-O coupling) rather than the Ir site (requiring 1.41 eV for O-O coupling). This makes O-O bond coupling step the rate-determining step (RDS) for OER over NCI-8.

These results indicate that both Ir and Co play essential bifunctional roles in the OER catalysis just as we found earlier for Fe-doped NiOOH [15, 45]. We see that the free energy barrier required for both the O radical formation and O-O coupling steps (0.49 and 1.18) are significantly reduced compared to the free energies required for OER in the NiOOH (2.06 eV) and the Fe-doped NiOOH (1.68 eV) [15]. These low energy barriers explain the observed enhanced catalytic performance for OER on NCI-8.

Table S4 compares NC with NCI-8, showing that without Ir, the 2nd step of forming the O radical character, is uphill by 1.50 eV compared to 0.49, showing the vital role of Ir in the OER process.

Moreover, increasing the content of Ir from 8% to 15% also decreases the catalytic activity of NCI, as shown experimentally in Fig. 5. To clarify why this increase in Ir content leads to lower catalytic activity than that of NCI-8, we carried out DFT calculation using a slab model of NCI-15 with an atomic ratio of 16.7% Ir in the NCI as shown in Fig. S19. The NCI-15 slab model was built by choosing the lowest energy model (where the additional Ir is located on the top surface of NCI-8) among five different cases assuming additional incorporation of Ir onto the top- or sub-surface of the NCI-8 model. We then examined the oxidation steps on the NCI-15 as for NCI-8, leading to the lowest OER pathway in Fig. 7.

We find that this increased concentration of Ir leads to a higher surface concentration of Ir in NCI-15, making the O radical formation step more endothermic by ~0.3 and the O-O coupling step more endothermic ~0.1 eV. Even more important, the higher concentration of Ir in NCI-15 makes desorption of O_2 product from its adsorption site on Co (O-O coupling on Co) more endothermic by ~0.2 eV (state 4 to state 5 in Fig. 7), which increases the onset potential and reduces the catalytic activity of the whole OER process.

These results demonstrate why NCI-8 exhibits the optimum OER activity among various NCI-x systems. Ir doping improves the OER activity of NC by stabilizing the O radical that helps O-O bond formation, but with a higher concentration of Ir on the surface, O_2 bonds too strongly decreasing overall OER activity.

3.4. Electrochemical characterization of catalysts

To further understand the superior OER performance of NCI-8, the electrochemical active surface area (ECSA) was calculated in terms of the double-layer capacitance (C_{dl}), but it should be noted here that the double-layer capacitance method does have some limitations in estimating the surface area, it may serve as diagnostic tools, but can't be accurately used for quantitative analysis. C_{dl} is measured by using CV measurements in a non-faradaic region near the open circuit potential. Fig. S20 shows the CV curves of the NiCo-based catalysts at different scan rates from 1 mV s^{-1} to 10 mV s^{-1}. The corresponding C_{dl} values are obtained through the equation: $C_{dl} = i / v$ (i is the charging current and v is the scan rate) [11]. As displayed in Fig. 8, the calculated C_{dl} value of NCI-8 is 5.59 mF cm^{-2}, which is much higher than that of NC (2.89 mF cm^{-2}), NCI-15 (3.71 mF cm^{-2}) and NCI-22 (3.61 mF cm^{-2}). In addition, the size of pre-OER redox waves can give insight into the electrochemically active surface area [11,46], we use the pre-OER Ni/Co-based redox couples as a way to estimate the number of electrolyte-accessible Ni/Co sites in our system, the results are shown in Fig. S21. It can be clearly observed that the increase in measured double-layer capacitance is related to the increased number of accessible metal redox sites. This suggests that NCI-8 has a large electrochemical surface area, which also provides plenty of active sites for electrochemical redox reactions [47], revealing the excellent OER activity.

Electrochemical impedance spectroscopy (EIS) tests were performed to investigate the kinetics of as-prepared electrocatalysts with different atomic ratios of Ir dopants under OER conditions. The Nyquist plots of NC, NCI-8, NCI-15 and NCI-22 are given in Fig. 9, which show two semicircles in the high and low frequency region, corresponding to the fast electron transfer process (resistance from substrate/catalyst interface) and charge transfer process (resistance from catalyst/electrolyte), respectively. The inset in Fig. 9a is the equivalent circuit of the Nyquist plots mentioned above, and the corresponding fitting results are shown

in Table S3. The charge transfer resistance (R_{ct}) of NCI-8 is obviously smaller than that of other as-prepared catalysts. It is measured to be only 0.42 Ω, indicating a faster charge transfer process for NCI-8 during the OER process. The extremely low value of R_{ct} is mainly due to the electronic structure modification derived from Ir doping, as well as the hierarchical porous structure of the catalyst and the good binding force between the ZnO/NCC substrate, all these factors contribute to the excellent OER performance of NCI-8.

3.5. Durability test

High durability of electrocatalyst is a key factor in the practical application. The galvanostatic method was utilized to evaluate the electrocatalytic durability of the as-fabricated NC, NCI-8, NCI-15 and NCI-22 by at 20 mA cm^{-2} (Fig. 10 and Fig. S22). We show that all as-fabricated electrocatalysts exhibit superior durability and well-maintained structure (Fig. S23), especially the overpotential of NCI-8 electrode increased only by 3% in the long-time 70 hour durability test, indicating that our fabricated NCI-8 electrode possess excellent durability in alkaline media, and is superior to previously reported other state-of-the-art catalytic Ni-Co-Ir, Co-Ir, Ni-Ir systems and electrodes (Table S2).

4. Conclusions

In order to develop efficient and durable electrocatalysts for the oxygen evolution reaction (OER), we designed a catalyst using mostly non-noble metal based materials to obtain excellent OER catalytic activity and durability. We synthesized Ir-doped NiCo oxyhydroxide (NCI) nanosheets with various concentrations of Ir using our novel photochemical deposition method. This leads to the deposition of catalyst layers with uniform and large catalytic active area with enhanced catalytic activity. We expect that the novel photochemical synthesis method developed here may provide improved catalysts for other applications.

Based on structural and electrochemical analysis, we found that the most efficient OER activity is for the NCI-8 nanosheets with 8% Ir and 46% Co. The net result is a current of 50 mA/cm^2 at a 260 mV overpotential, one of the best OER performance reported so far. Moreover, NCI-8 leads to stable performance at a current of 20 mA cm^{-2} for 70 hours in alkaline media.

Our DFT calculations support the experimental results showing that OER on NCI-8 is faster than on NC, because the barrier for forming O radical character on the Ir is much lower while for NCI-15 the product O_2 is too stable to desorb. These results show that Ir and Co play synergetic roles in this catalyst.

Declaration of competing interest

The authors declare that they have no known competing financial interests or personal relationships that could have appeared to influence the work reported in this paper.

Acknowledgements.

The Zhejiang University part of this research was supported by the National Natural Science Foundation of China (No. 21373182) and the Zhejiang Provincial Natural Science Foundation of China (LY17B030004). The research in Korea was supported by the National Research Foundation of Korea (NRF) grant funded by the Korea government (MSIT) (No.

433 2020R1C1C1008458). The Caltech portion of the work was supported by the the US National
434 Sicene Founation (CBET-1805022, Bob McCabe program manager).

435

436 **Appendix A. Supplementary data.**

437 Supplementary data associated with this article can be found online at doi:xxx.

438

References

[1] M.G. Walter, E.L. Warren, J.R. McKone, S.W. Boettcher, Q.X. Mi, E.A. Santori, N.S. Lewis, Solar water splitting cells, Chem. Rev. 110 (2010) 6446–6473. https://doi.org/10.1021/cr1002326.

[2] T.R. Cook, D.K. Dogutan, S.Y. Reece, Y. Surendranath, T.S. Teets, D.G. Nocera, Solar energy supply and storage for the legacy and nonlegacy worlds, Chem. Rev. 110 (2010) 6474–6502. https://doi.org/10.1021/cr100246c.

[3] J. Suntivich, K.J. May, H.A. Gasteiger, J.B. Goodenough, Y. Shao-Horn, A perovskite oxide optimized for oxygen evolution catalysis from molecular orbital principles, Science 334 (2011) 1383–1385. https://doi.org/10.1126/science.1212858.

[4] B. Zhang, X. Zheng, O. Voznyy, R. Comin, M. Bajdich, M.G. Melchor, L. Han, J. Xu, M. Liu, L. Zheng, F.P.G. Arquer, C.T. Dinh, F. Fan, M. Yuan, E. Yassitepe, N. Chen, T. Regier, P. Liu, Y. Li, P. Luna, A. Janmohamed, H.L. Xin, H. Yang, A. Vojvodic, E.H. Sargent, Homogeneously dispersed multimetal oxygen-evolving catalysts, Science 352 (2016) 333–337. https://doi.org/10.1126/science.aaf1525.

[5] Y. Jin, S. Huang, X. Yue, H. Du, P.K. Shen, Mo- and Fe-modified $Ni(OH)_2$/NiOOH nanosheets as highly active and stable electrocatalysts for oxygen evolution reaction, ACS Catal. 8 (2018) 2359–2363. https://doi.org/10.1021/acscatal.7b04226.

[6] M. Gao, W. Sheng, Z. Zhuang, Q. Fang, S. Gu, J. Jiang, Y. Yan, Efficient water oxidation using nanostructured α- nickel-hydroxide as an electrocatalyst, J. Am. Chem. Soc. 136 (2014) 7077–7084. https://doi.org/10.1021/ja502128j.

[7] A. Nadeema, V.M. Dhavale, S. Kurungot, NiZn double hydroxide nanosheet-anchored nitrogen-doped graphene enriched with the γ-NiOOH phase as an activity modulated water oxidation electrocatalyst, Nanoscale 9 (2017) 12590-12600. https://doi.org/10.1039/c7nr02225e.

[8] D.K. Bediako, B. Lassalle-Kaiser, Y. Surendranath, J. Yano, V.K. Yachandra, D.G. Nocera, Structure-activity correlations in a nickel-borate oxygen evolution catalyst, J. Am. Chem. Soc. 134 (2012) 6801–6809. https://doi.org/10.1021/ja301018q.

[9] L. Trotochaud, S.L. Young, J.K. Ranney, S.W. Boettcher, Nickel-iron oxyhydroxide oxygen-evolution electrocatalysts: the role of intentional and incidental iron incorporation, J. Am. Chem. Soc. 136 (2014) 6744–6753. https://doi.org/10.1021/ja502379c.

[10] M. Görlin, P. Chernev, J.F. Araújo, T. Reier, S. Dresp, B. Paul, R. Krähnert, H. Dau, P. Strasser, Oxygen evolution reaction dynamics, faradaic charge efficiency, and the active metal redox states of Ni-Fe oxide water splitting electrocatalysts, J. Am. Chem. Soc. 138 (2016) 5603–5614. https://doi.org/10.1021/jacs.6b00332.

[11] M.B. Stevens, L.J. Enman, A.S. Batchellor, M.R. Cosby, A.E. Vise, C.D.M. Trang, S.W. Boettcher, Measurement techniques for the study of thin film heterogeneous water oxidation electrocatalysts, Chem. Mater. 29 (2017) 120–140. https://doi.org/10.1021/acs.chemmater.6b02796.

[12] X.D. Jia, Y.F. Zhao, G.B. Chen, L. Shang, R. Shi, X.F. Kang, G.I.N. Waterhouse, L.Z. Wu, C.H. Tung, T.R. Zhang, Ni_3FeN nanoparticles derived from ultrathin NiFe-layered double hydroxide nanosheets: an efficient overall water splitting electrocatalyst, Adv. Energy Mater. 6 (2016) 1502585. https://doi.org/10.1002/aenm.201502585.

[13] A.L. Wang, Y.T. Dong, M. Li, C.L. Liang, G.R. Li, In situ derived $Ni_xFe_{1-x}OOH/NiFe/Ni_xFe_{1-x}OOH$ nanotube arrays from NiFe alloys as efficient electrocatalysts for oxygen evolution, ACS Appl. Mater. Interfaces 9 (2017) 34954–34960. https://doi.org/10.1021/acsami.7b10609.

[14] C. Tang, H.S. Wang, H.F. Wang, Q. Zhang, G.L. Tian, J.Q. Nie, F. Wei, Spatially confined hybridization of nanometer-sized NiFe hydroxides into nitrogen-doped graphene frameworks leading to superior oxygen evolution reactivity, Adv. Mater. 27 (2015) 4516–4522. https://doi.org/10.1002/adma.201501901.

[15] H. Shin, H. Xiao, W.A. Goddard, In silico discovery of new dopants for Fe-doped Ni oxyhydroxide ($Ni_{1-x}Fe_xOOH$) catalysts for oxygen evolution reaction, J. Am. Chem. Soc. 140 (2018) 6745–6748. https://doi.org/10.1021/jacs.8b02225.

[16] R.D.L. Smith, M.S. Prévot, R.D. Fagan, Z. Zhang, P.A. Sedach, M.K.J. Siu, S. Trudel, C.P. Berlinguette, Photochemical route for accessing amorphous metal oxide materials for water oxidation catalysis, Science 340 (2013) 60–63. https://doi.org/10.1126/science.1233638.

[17] R.D.L. Smith, B. Sporinova, R.D. Fagan, S. Trudel, C.P. Berlinguette, Facile photochemical preparation of amorphous iridium oxide films for water oxidation catalysis, Chem. Mater. 26 (2014) 1654–1659. https://doi.org/10.1021/cm4041715.

[18] R.D.L. Smith, M.S. Prévot, R.D. Fagan, S. Trudel, C.P. Berlinguette, Water oxidation catalysis: electrocatalytic response to metal stoichiometry in amorphous metal oxide films containing iron, cobalt, and nickel, J. Am. Chem. Soc. 135 (2013) 11580–11586. https://doi.org/10.1021/ja403102j.

[19] W. Qiu, Y. Li, A. You, Z. Zhang, G. Li, X. Lu, Y. Tong, High-performance flexible quasi-solid-state Zn-MnO_2 battery based on MnO_2 nanorod arrays coated 3D porous nitrogen-doped carbon cloth, J. Mater. Chem. A 5 (2017) 14838–14846. https://doi.org/10.1039/C7TA03274A.

[20] B.J. Waghmode, A.P. Gaikwad, C.V. Rode, S.D. Sathaye, K.R. Patil, D.D. Malkhede, Calixarene intercalated NiCo layered double hydroxide for enhanced oxygen evolution catalysis, ACS Sustainable Chem. Eng. 6 (2018) 9649–9660. https://doi.org/10.1021/acssuschemeng.7b04788.

[21] G. Kresse, J. Furthmüller, Efficient iterative schemes for ab initio total-energy calculations using a plane-wave basis set, J. Phys. Rev. B 54 (1996) 11169–11186. https://doi.org/10.1103/PhysRevB.54.11169.

[22] J.P. Perdew, K. Burke, M. Ernzerhof, Generalized gradient approximation made simple, Phys. Rev. Lett. 77 (1996) 3865–3868. https://doi.org/10.1103/physrevlett.77.3865.

[23] P.E. Blöchl, Projector augmented-wave method, Phys. Rev. B 50 (1994) 17953–17979. https://doi.org/10.1103/PhysRevB.50.17953.

[24] H.K. Lim, H. Shin, W.A. Goddard, Y.J. Hwang, B.K. Min, H. Kim, Embedding covalency into metal catalysts for efficient electrochemical conversion of CO_2, J. Am. Chem. Soc. 136 (2014) 11355–11361. https://doi.org/10.1021/ja503782w.

[25] H. Shin, Y. Ha, H. Kim, 2D covalent metals: a new materials domain of electrochemical CO_2 conversion with broken scaling relationship, J. Phys. Chem. Lett. 7 (2016) 4124–4129. https://doi.org/10.1021/acs.jpclett.6b01876.

[26] S. Yook, H. Shin, H. Kim, M. Choi, Selective dissociation of dihydrogen over dioxygen on a hindered platinum surface for the direct synthesis of hydrogen peroxide, Chemcatchem, 6 (2014) 2836–2842. https://doi.org/10.1002/cctc.201402436.

[27] T. Reier, H.N. Nong, D. Teschner, R. Schlögl, P. Strasser, Electrocatalytic oxygen evolution reaction in acidic environments-reaction mechanisms and catalysts, Adv. Energy Mater. 7 (2017) 1601275. https://doi.org/10.1002/aenm.201601275.

[28] D. Chandra, D. Takama, T. Masaki, T. Sato, N. Abe, T. Togashi, M. Kurihara, K. Saito, T. Yui, M. Yagi, Highly efficient electrocatalysis and mechanistic investigation of intermediate $IrO_x(OH)_y$ nanoparticle films for water oxidation, ACS Catal. 6 (2016) 3946–3954. https://doi.org/10.1021/acscatal.6b00621.

[29] O.D. Morales, T. Hersbach, D. Hetterscheid, J. Reek, M. Koper, Electrochemical and spectroelectrochemical characterization of an iridium-based molecular catalyst for water splitting: turnover frequencies, stability, and electrolyte effects, J. Am. Chem. Soc. 136 (2014) 10432–10439. https://doi.org/10.1021/ja504460w.

[30] K. Joya, X. Sala, In situ Raman and surface-enhanced Raman spectroscopy on working electrodes: spectroelectrochemical characterization of water oxidation electrocatalysts, Phys. Chem. Chem. Phys. 17 (2015) 21094–21103. https://doi.org/10.1039/C4CP05053C.

[31] H. Moussa, E. Girot, K. Mozet, H. Alem, G. Medjahdi, R. Schneider, ZnO rods/reduced graphene oxide composites prepared via a solvothermal reaction for efficient sunlight-driven photocatalysis, Appl. Catal. B: Environ. 185 (2016) 11–21. https://doi.org/10.1016/j.apcatb.2015.12.007.

[32] Y.K. Mishra, G. Modi, V. Cretu, V. Postica, O. Lupan, T. Reimer, I. Paulowicz, V. Hrkac, W. Benecke, L. Kienle, R. Adelung, Direct growth of freestanding ZnO tetrapod networks for multifunctional applications in photocatalysis, UV photodetection, and gas sensing, ACS Appl. Mater. Interfaces 7 (2015) 14303–14316. https://doi.org/10.1021/acsami.5b02816.

[33] J.A. Koza, C.M. Hull, Y.C. Liu, J.A. Switzer, Deposition of β-$Co(OH)_2$ films by electrochemical reduction of tris(ethylenediamine)cobalt(III) in alkaline solution, Chem. Mater. 25 (2013) 1922–1926. https://doi.org/10.1021/cm400579k.

[34] Y. Li, L. Hu, W. Zheng, X. Peng, M. Liu, P.K. Chu, L.Y. Lee, Ni/Co-based nanosheet arrays for efficient oxygen evolution reaction, Nano Energy 52 (2018) 360–368. https://doi.org/10.1016/j.nanoen.2018.08.010.

[35] M. Steimecke, G. Seiffarth, M. Bron, In situ characterization of Ni and Ni/Fe thin film electrodes for oxygen evolution in alkaline media by a Raman-coupled scanning electrochemical microscope setup, Anal. Chem. 89 (2017) 10679–10686. https://doi.org/10.1021/acs.analchem.7b01060.

[36] B.S. Yeo, A.T. Bell, In situ Raman study of nickel oxide and gold-supported nickel oxide catalysts for the electrochemical evolution of oxygen, J. Phys. Chem. C 116 (2012) 8394–8400. https://doi.org/10.1021/jp3007415.

[37] G.C. Silva, M.R. Fernandes, E.A. Ticianelli, Activity and stability of Pt/IrO_2 bifunctional materials as catalysts for the oxygen evolution/reduction reactions, ACS Catal. 8 (2018) 2081–2092. https://doi.org/10.1021/acscatal.7b03429.

[38] H.G.S. Casalongue, M.L. Ng, S. Kaya, D. Friebel, H. Ogasawara, A. Nilsson, In situ observation of surface species on iridium oxide nanoparticles during the oxygen evolution reaction, Angew. Chem. Int. Ed. 53 (2014) 7169–7172. https://doi.org/10.1002/anie.201402311.

[39] L.S. Sharninghausen, S.B. Sinha, D.Y. Shopov, B.Q. Mercado, D. Balcells, G.W. Brudvig, R.H. Crabtree, Synthesis and characterization of iridium(V) coordination complexes with an N,O-donor organic ligand, Angew. Chem. 129 (2017) 13227–13231. https://doi.org/10.1002/anie.201707593.

[40] N. Li, D.K. Bediako, R.G. Hadt, D. Hayes, T.J. Kempa, F.V. Cube, D.C. Bell, L.X. Chen, D.G. Nocera, Influence of iron doping on tetravalent nickel content in catalytic oxygen evolving films, Proc. Natl. Acad. Sci. USA 114 (2017) 1486–1491. https://doi.org/10.1073/pnas.1620787114.

[41] J. Huang, J. Chen, T. Yao, J. He, S. Jiang, Z. Sun, Q. Liu, W. Cheng, F. Hu, Y. Jiang, Z. Pan, S. Wei, CoOOH nanosheets with high mass activity for water oxidation, Angew. Chem. Int. Ed. 54 (2015) 8722–8727. https://doi.org/10.1002/anie.201502836.

[42] F. Song, X. Hu, Ultrathin cobalt-manganese layered double hydroxide is an efficient oxygen evolution catalyst, J. Am. Chem. Soc. 136 (2014) 16481–16484. https://doi.org/10.1021/ja5096733.

[43] S. Zou, M.S. Burke, M.G. Kast, J. Fan, N. Danilovic, S.W. Boettcher, Fe (oxy)hydroxide oxygen evolution reaction electrocatalysis: intrinsic activity and the roles of electrical conductivity, substrate, and dissolution, Chem. Mater. 27 (2015) 8011–8020. https://doi.org/10.1021/acs.chemmater.5b03404.

[44] C. Wei, R.R. Rao, J. Peng, B. Huang, I.E.L. Stephens, M. Risch, Z.J. Xu, Y.S. Horn, Recommended practices and benchmark activity for hydrogen and oxygen electrocatalysis in water splitting and fuel cells, Adv. Mater. 31 (2019) 1806296. https://doi.org/10.1002/adma.201806296.

[45] H. Xiao, H. Shin, W.A. Goddard, Synergy between Fe and Ni in the optimal performance of (Ni,Fe)OOH catalysts for the oxygen evolution reaction, Proc. Natl. Acad. Sci. USA 115 (2018) 5872–5877. https://doi.org/10.1073/pnas.1722034115.

[46] S. Trasatti, O.A. Petrii, Real surface area measurements in electrochemistry, J. Electroanal. Chem. 327 (1992) 353–376. https://doi.org/10.1016/0022-0728(92)80162-W.

[47] D. Zhong, L. Zhang, C. Li, D. Li, C. Wei, Q. Zhao, J. Li, J. Gong, Nanostructured NiFe (oxy)hydroxide with easily oxidized Ni towards efficient oxygen evolution reactions, J. Mater. Chem. A 6 (2018) 16810–16817. https://doi.org/10.1039/C8TA04721A.

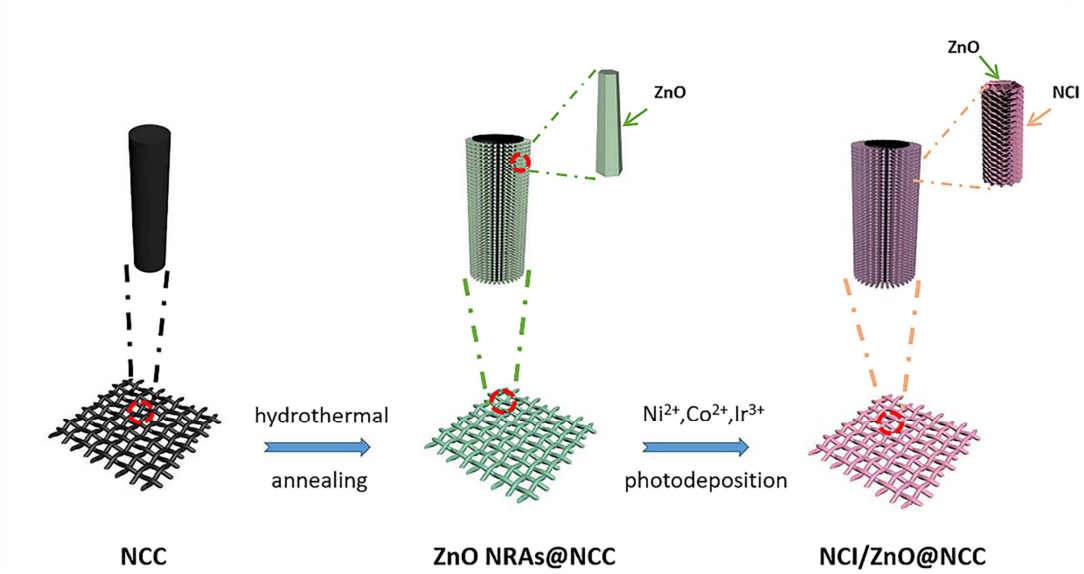

603

604 **Fig. 1.** Schematic illustration for the fabrication of hierarchical layered Ir-doped
605 NiCoOOH/ZnO@NCC composite film.

606

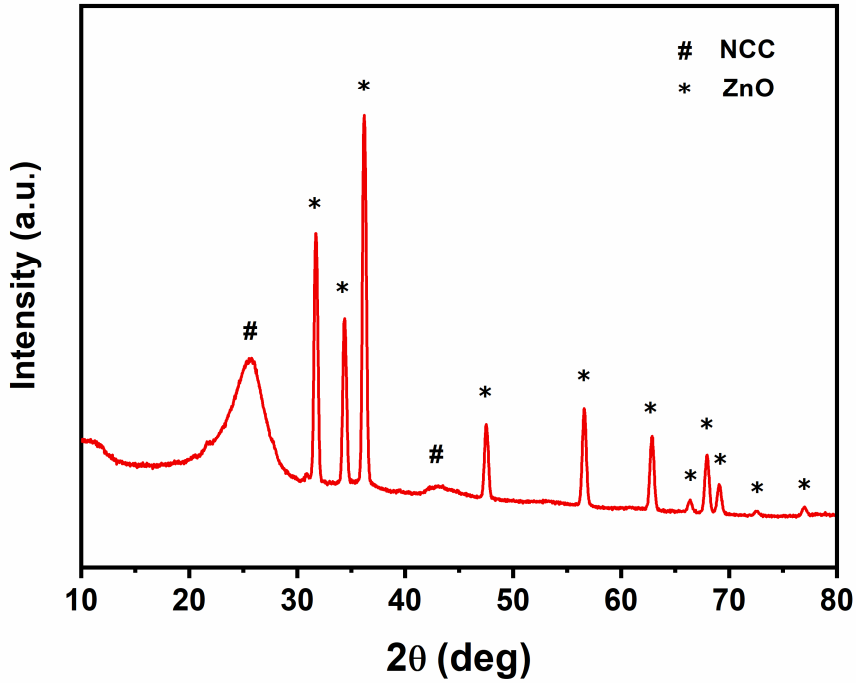

Fig. 2. XRD pattern of the as-fabricated NCI-8.

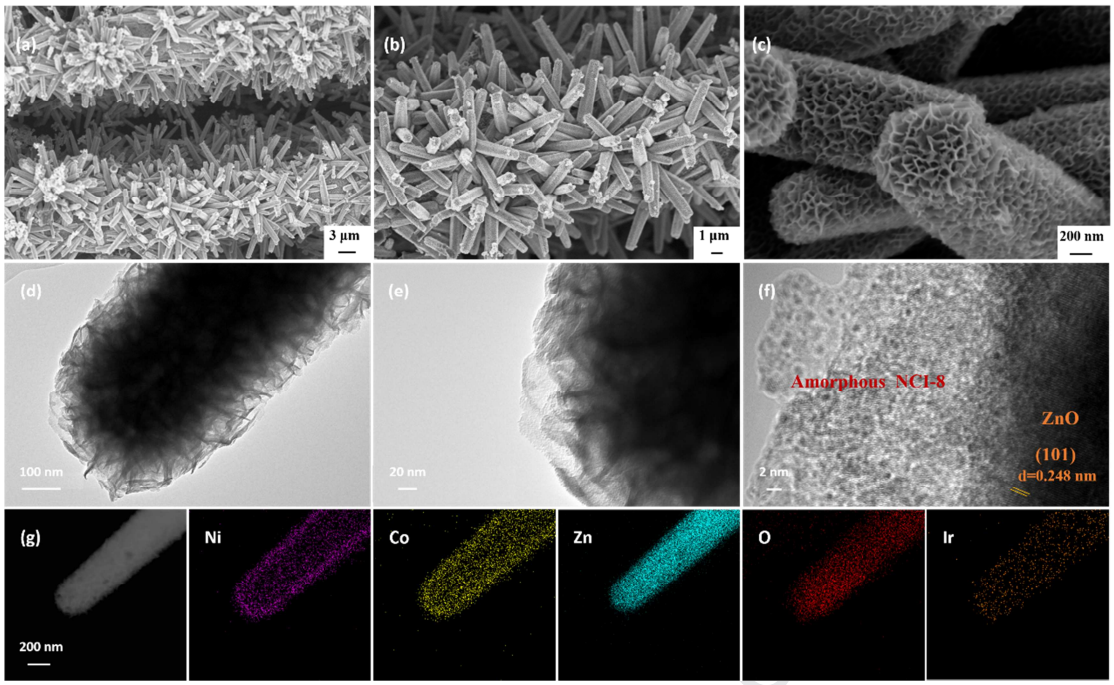

Fig. 3. (a-c) SEM, (d, e) TEM and (f) HRTEM images of NCI-8. (g) Elemental mappings of Ni, Co, Zn, O and Ir in NCI-8.

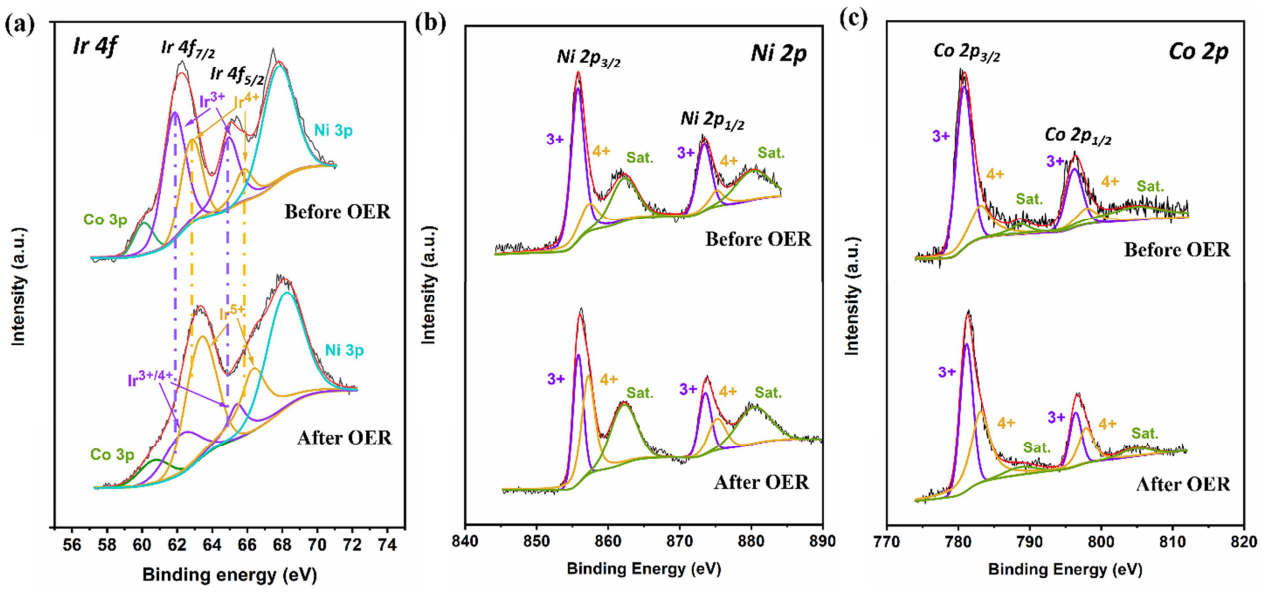

Fig. 4. High-resolution XPS patterns of NCI-8 before and after OER. (a) Ir 4*f*, (b) Ni 2*p* and (c) Co 2*p*.

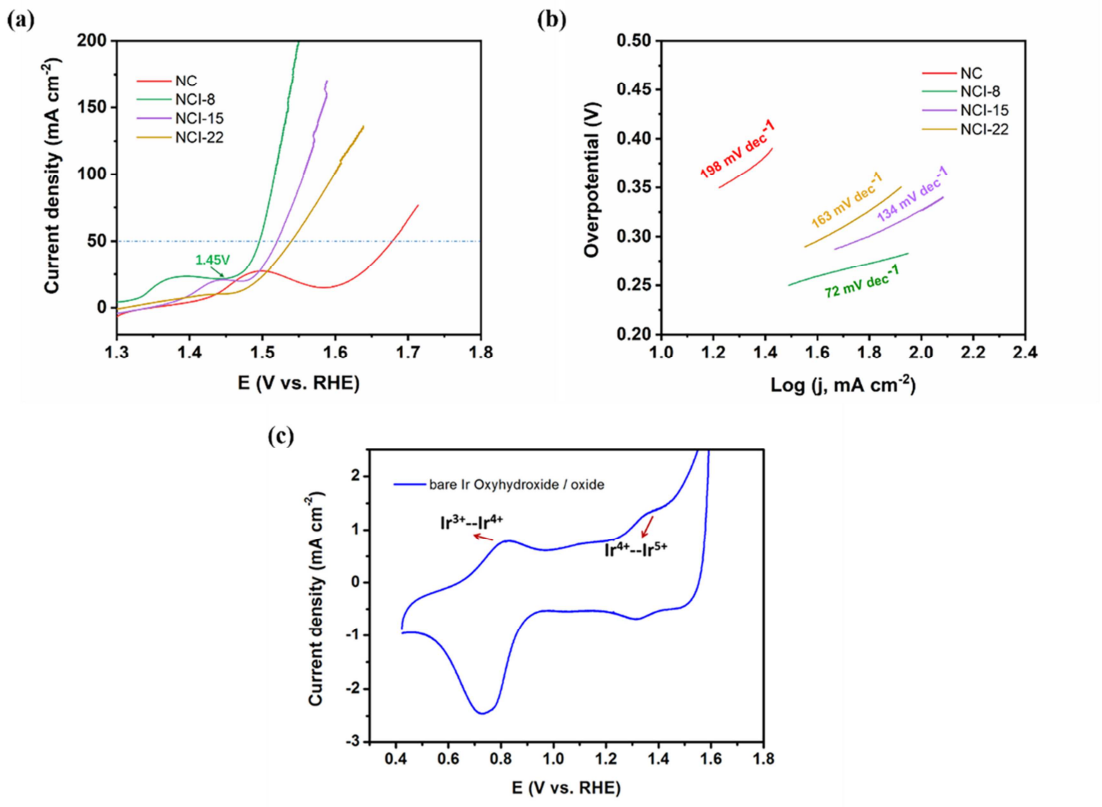

629

630 **Fig. 5.** (a) LSV curves of NC, NCI-8, NCI-15 and NCI-22 for OER at a scan rate of 5 mV s^{-1}
631 in 1 M KOH; (b) The corresponding Tafel plots; (c) the CV curve of bare Ir
632 oxyhydroxide/oxide at 5 mV s^{-1} in 1 M KOH.

633

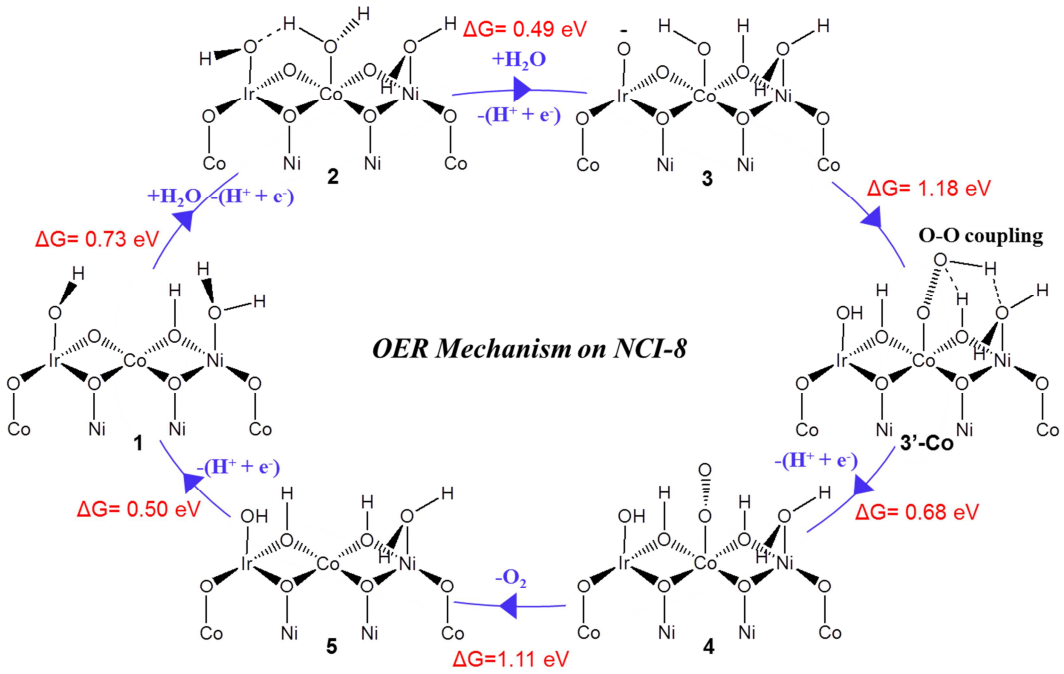

Fig. 6. Mechanism for OER on NCI-8 catalyst.

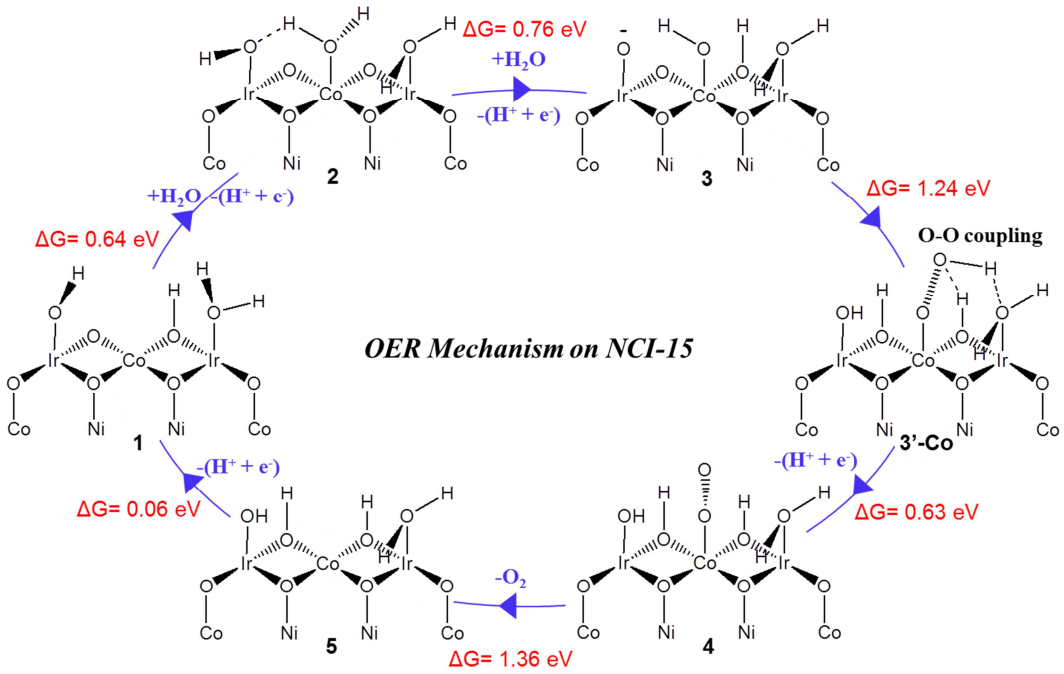

637

638 **Fig. 7.** Mechanism for OER on NCI-15 catalyst.

639

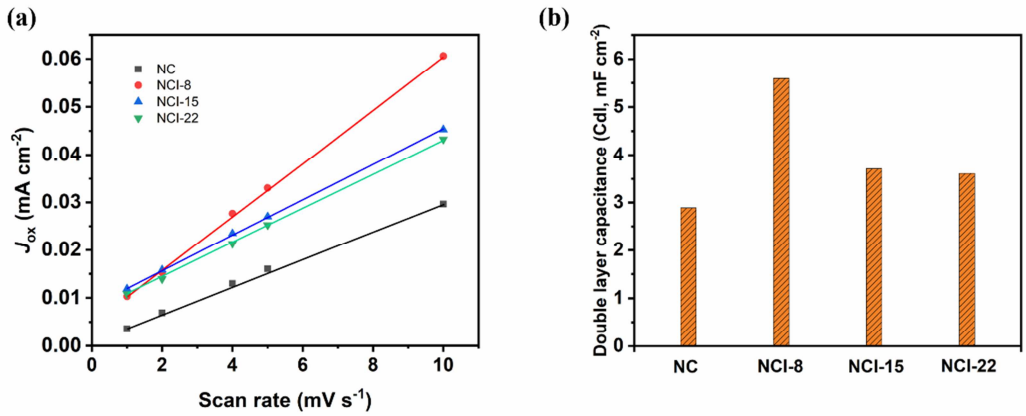

Fig. 8. (a) The relationship between scan rate and charge current density of double layer capacitor and (b) the corresponding electrochemical double-layer capacitances of NC, NCI-8, NCI-15 and NCI-22.

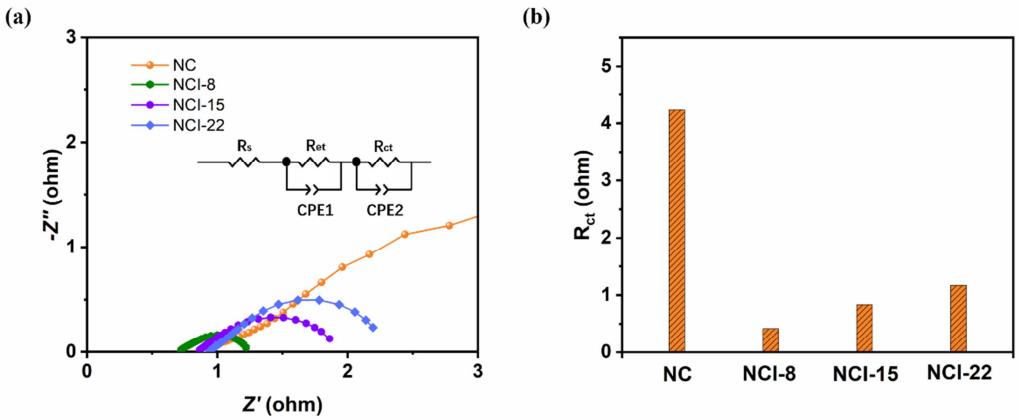

Fig. 9. Nyquist plots (a) and charge transfer resistance (b) of NC, NCI-8, NCI-15 and NCI-22 at 1.54 V vs. RHE. Inset in Fig. 9a is the corresponding equivalent circuit model for the Nyquist plots.

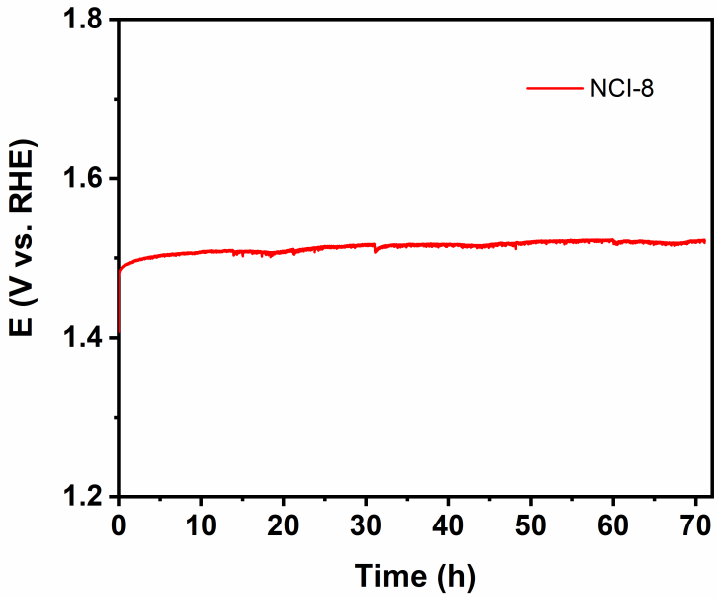

650

651 **Fig. 10.** Durability test at 20 mA cm^{-2} for 70 hours of NCI-8 electrode.

652

Liang-ai Huang received her B.S. degree in Applied Chemistry (2014) from Sha oxing University. Currently, she is a Ph.D. candidate in Zhejiang University. Her research interests are mainly focused on electrochemical catalysis.

Hyeyoung Shin is an assistant professor at the Graduate School of Energy Science and Technology (GEST), Chungnam National University, Korea. She received her PhD in theoretical chemistry from Korea Advanced Institute of Science and Technology (KAIST) in 2016. Her main research interests focus on developing new materials and its application to renewable energy systems.

William A. Goddard III is Charles and Mary Ferkel Professor of Chemistry, Materials Science, and Applied Physics and Director of the Materials and Process Simulation Center at the California Institute of Technology (Caltech), Pasadena CA USA. He received his PhD in Engineering Science from Caltech in 1965 and has been on the faculty at Caltech since then. His research interests are developing new methods of quantum mechanics (QM) and of QM based multiscale methods and in applied these methods to developing new catalysts, materials, and pharma.

Jianming Wang is a professor in Department of Chemistry, Zhejiang University, P.R. China. He received his Ph.D. degree in Institute of Metal Corrosion and Protection, Chinese Academy of Sciences in 1996. His research interests are focused on electrochemical power sources, electrochemical catalysis, photoelectrochemistry and corrosion.

Highlights

- Ir-doped NiCo oxyhydroxide nanosheets with 8% Ir and 46% Co (NCI-8) are synthesized using novel photodeposition method that producing uniform and large catalytic active area leading to enhanced catalytic activity.
- NCI-8 shows the best performance for the oxygen evolution reaction (OER) activity, leading to 50 mA cm^{-2} at an overpotential of 260 mV, which provides stable performance for 70 hours in alkaline media.
- Ir and Co play essential bifunctional roles in stabilizing the key O radical intermediate on Ir and promoting the O-O bond coupling on Co, respectively.

Declaration of interests

☒ The authors declare that they have no known competing financial interests or personal relationships that could have appeared to influence the work reported in this paper.